

A Rayleigh Mixture Model for IVUS Imaging

José Seabra, Francesco Ciompi, Petia Radeva, and João Miguel Sanches

Abstract Carotid and coronary vascular problems, such as heart attack or stroke, are often originated in vulnerable plaques. Hence, the accurate characterization of plaque echogenic contents could help in diagnosing such lesions.

The Rayleigh distribution is widely accepted as an appropriate model to describe plaque morphology although it is known that other more complex distributions depending on multiple parameters are usually needed whenever the tissues show significant heterogeneity.

In this chapter a new model to describe the tissue echo-morphology by using a mixture of Rayleigh distribution is described. This model, called *Rayleigh Mixture Model* (RMM), combines the robustness of a mixture model with the mathematical simplicity and adequacy of the Rayleigh distributions to deal with the *speckle* multiplicative noise that corrupts the ultrasound images.

The method for the automatic estimation of the RMM mixture parameters by using the *Expectation Maximization* (EM) algorithm is described.

The performance of the proposed model is evaluated with a database of in-vitro IVUS samples. We show that the mixture coefficients and Rayleigh parameters explicitly derived from the mixture model are able to accurately describe different plaque types and to significantly improve the characterization performance of an already existing methodology.

J. Seabra (✉) • J.M. Sanches

Institute for Systems and Robotics, Department of Bioengineering from the Instituto Superior Técnico/Technical University of Lisbon, Portugal
e-mail: mail2jseabra@gmail.com; jmrs@ist.utl.pt

F. Ciompi • P. Radeva

Computer Vision Center, Campus UAB, Edifici O, Bellaterra, Spain

University of Barcelona, Gran Via de Les Cortes Catalanes, 585, 08007 Barcelona, Spain
e-mail: fciompi@maia.ub.es; petia@cvc.uab.es

1 Introduction

Atherosclerotic plaques may eventually present high risk of rupture, consequently leading to brain stroke or heart attack [1]. Albeit vulnerable plaque is a concept well accepted as a clinical entity with potential harmful consequences, its echo-morphology, and pathological evolution it is not yet well understood. Hence, it is important to objectively characterize the plaque echo-morphology to identify this kind of lesions and develop or refine methods for risk prediction.

Ultrasound images are corrupted by a characteristic granular pattern, called *speckle* [2], that depends on the number of scatterers (reflectors) as well as their size. This speckle signal is usually considered noise and there is a lot of work in the literature proposing methods to its removal [3–6]. However, *speckle* encodes information about tissue acoustic properties [7] that can be used for diagnostic purposes.

As pointed out in [8], features extracted from these noisy images can be considered as tissue histological descriptors. Moreover, IVUS is an imaging technique which enables to clearly assess the arterial wall internal echo-morphology. The technical procedure of acquiring IVUS data consists in introducing a catheter, carrying a rotating ultrasound emitter inside the vessel. During rotation, a piezoelectric transducer transmits US waves and collects the reflected components which are afterward converted into electrical signals (A-lines) and sampled by an Analog to Digital Converter (see Fig. 1b). The IVUS image is obtained by processing the received echoes is a 360-degree tomographic view of the inner arterial walls (Fig. 1a). The proximity of the ultrasound probe from the inner arterial walls makes

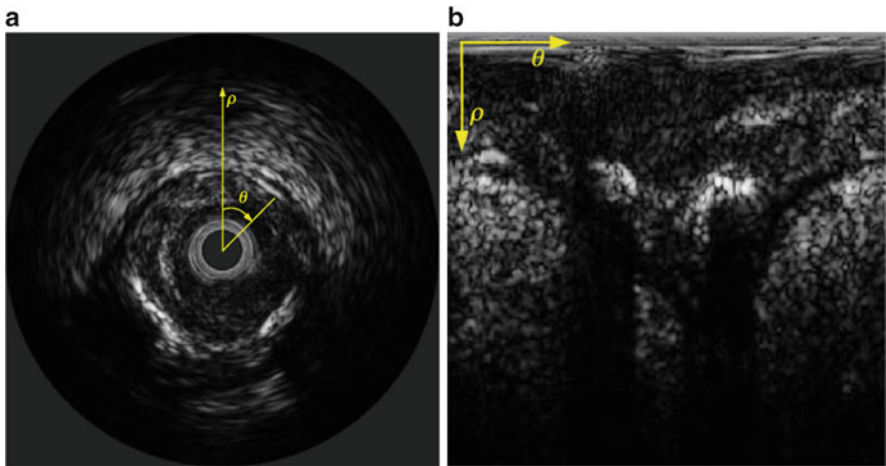


Fig. 1 (a) IVUS image represented in cartesian coordinates and (b) its corresponding polar representation; ρ represents the depth in the tissue and θ the position (angle) in the rotation of the probe

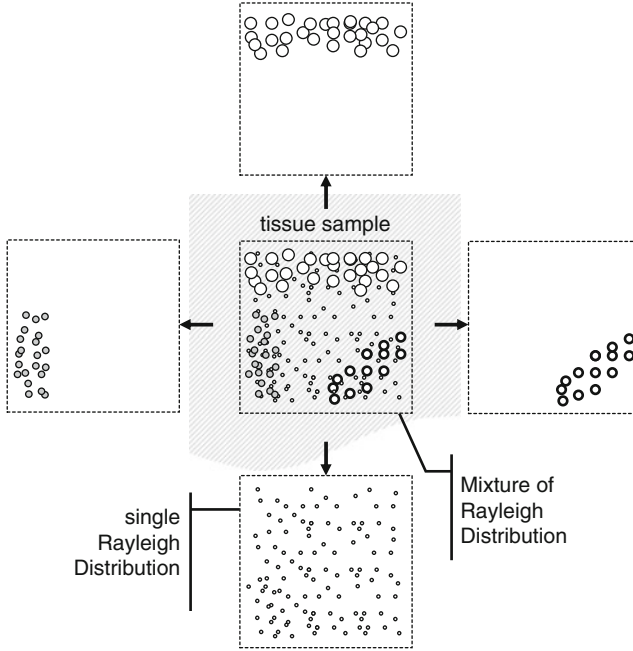


Fig. 2 Hypothetical acoustic tissue model, including different scattering phenomena which points out the need for using a mixture model of distributions

it possible to use high frequency US probes and therefore obtain high quality US images. Consequently, IVUS is commonly considered a suitable technique for accurate *in-vivo* characterization of the coronary plaques composition [9].

Studies which rely on tissue appearance [10, 11] were pursued to qualitatively and subjectively characterize plaque echo-morphology as soft (echolucent), fibrous (intermediate echogenicity), mixed (several acoustical subtypes), and calcified (strongly echogenic). Given the high variability in tissue appearance, the IVUS imaging parameters (such as brightness and contrast) are often tuned to improve visualization. This pre-processing operation modifies the IVUS signal properties, hinders the comparison of tissues on different images and prevents the application of appearance-based methods. Thus, analysis from RF data is needed to obtain discrimination of plaques. Recently, automatic quantitative methods for plaque characterization have been proposed, based either on high-order statistical texture analysis [12–14] and on spectral features extracted from the raw RF signals acquired by the IVUS equipment [15–17].

The work presented in this chapter aims to model the atherosclerotic plaque through the analysis of the envelope backscattered IVUS data. For this purpose, an hypothetical model is considered where a scanned tissue sample suffers from a certain number of scattering phenomena, as depicted in Fig. 2.

The commonest model for speckle formation is known as fully [18] and considers a tissue or region composed by a large number of scatterers, acting as echo reflectors. These scatterers arise from structural inhomogeneities with size approximately equal or smaller than the wavelength of the ultrasound, such as in the parenchyma, where there are changes in acoustic impedance on a microscopic level within the tissue. Under fully developed speckle, pixel intensities in envelope images are well modeled by Rayleigh PDFs [2, 19]. When this condition does not hold, other more complex parametric models, such as K [20], Rician [21], homodyned-K [22], and Nakagami [23] are suitable to describe the data.

The motivation to use the single parameter Rayleigh distribution comes from the fact that the regions defining atherosclerotic tissue are piecewise homogeneous and do not present strong scatterers nor edges, as it happens across the rest of the image, where other speckle conditions are verified and other statistical models are more convenient. These other models, such as Rice, K or Nakagami distributions, depend on a large number of parameters which makes the estimation of tissue echo-morphology a hard task.

Plaque echo-morphology may result from different types of components, spatial organization, and complexity which determine different scattering phenomena where the Rayleigh distribution would be a reasonable approximation but a compound statistical model would be more appropriate. Hence, the description of tissue echo-morphology may be tackled with complex distributions depending on multiple parameters or with a mixture of simple distributions. In this chapter a combination of Rayleigh distributions, called *Rayleigh Mixture Model* (RMM), is proposed to describe the tissue echo-morphology in atherosclerotic plaques from IVUS images. The coefficients of the mixture are estimated with the *Expectation Maximization* (EM) algorithm [24] adapted to this kind of mixture.

The RMM consists of a technique to describe a particular data distribution by linearly combining different Rayleigh PDFs. Up to our knowledge, the RMM was never used for tissue characterization in ultrasound, although these models have been successfully employed in other fields, such as in underwater acoustics and speech processing problems [25, 26].

This chapter is organized as follows. First, in Sect. 2.1 a comprehensive mathematical formulation of the mixture model is provided, using the EM algorithm for estimating the coefficients and Rayleigh parameters of the mixture. Second, the adequacy of the proposed model to describe the envelope ultrasound data is evaluated on validated IVUS data of different plaque types (Sect. 3.3). Moreover, the RMM is applied for modeling plaques as monolithic objects, i.e., by considering all the pixels enclosed in the plaque. The features explicitly obtained from the mixture model (cf. Sect. 2.1) are used to investigate the discriminative power of the model for identifying different tissue types, namely fibrotic, lipidic, and calcified ones. In Sect. 3.4 the ability of the RMM for pixel-wise classification of plaque composition is evaluated when using only the proposed features and when combining them with textural and spectral features recently proposed [27]. Finally, we investigate the significance of the obtained classification improvement when using the RMM features (cf. Sects. 3.5 and 3.6).

2 Methods

In this section a mathematical formulation of the problem is provided and the estimation algorithm for the coefficients of the mixture (weights) and Rayleigh parameters of each component, by using the EM algorithm, is described.

2.1 Rayleigh Mixture Model

Let $Y = \{y_i\}$, $1 \leq i \leq N$, be a set of pixel intensities of a given region of interest, particularly a plaque, from an ultrasound image. Pixel intensities are considered random variables which are described by the following mixture of L distributions

$$p(y_i|\Psi) = \sum_{j=1}^L \theta_j \phi_j(y_i), \quad (1)$$

where $\Psi = (\theta_1, \dots, \theta_L, \sigma_1, \dots, \sigma_L)$ is the vector of parameters to estimate. θ_j are the coefficients of the mixture and σ_j are the parameters of each Rayleigh component, $\phi_j(y_i) = p(y_i|\sigma_j)$,

$$p(y_i|\sigma_j) = \frac{y_i}{\sigma_j^2} \exp\left(-\frac{y_i^2}{2\sigma_j^2}\right), \quad (2)$$

The condition $\sum_{j=1}^L \theta_j = 1$ must hold to guarantee that $p(y_i|\Psi)$ is a true distribution function.

The parameters σ_j associated with the pixel intensity y_i , characterize the acoustic properties of the tissue at the i th location [28]. The effect of changing σ in the shape of the distribution and thus in the image intensity is illustrated in Fig. 3. The joint distribution of the pixel intensities, considered independent and identically distributed (i.i.d.), is given by,

$$p(\mathbf{Y}|\Psi) = \prod_i^N p(y_i|\Psi). \quad (3)$$

The goal is to estimate Ψ by maximizing the *likelihood* function,

$$\hat{\Psi}_{\text{ML}} = \arg \max_{\Psi} \mathcal{L}(\mathbf{Y}, \Psi), \quad (4)$$

where

$$\mathcal{L}(\mathbf{Y}, \Psi) = \log p(\mathbf{Y}|\Psi) = \sum_{i=1}^N \log \left(\sum_{j=1}^L \theta_j p_j(y_i|\sigma_j) \right). \quad (5)$$

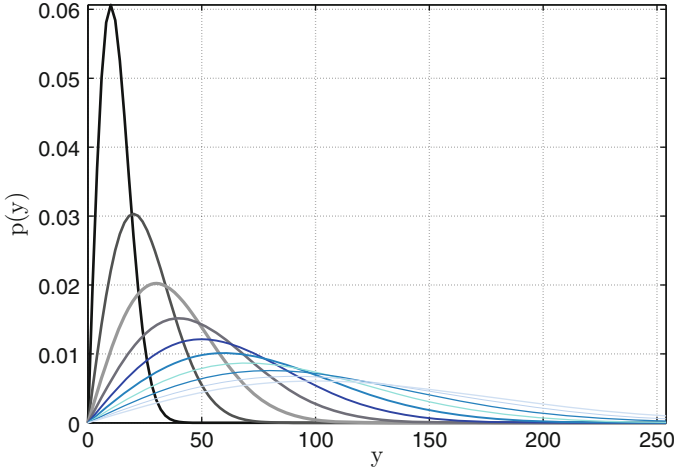


Fig. 3 Rayleigh PDFs generated with parameter $10^2 < \sigma < 10^3$ (from darker to lighter curves)

The maximization of (5) is a difficult task because it consists of a logarithmic function of a sum of terms. To overcome this difficulty the EM [24] method is used where a set of hidden variables are introduced, $K = \{k_i\}$ with $k_i \in \{1, \dots, L\}$. The value of $k_i = j$ informs us about the mixture component j that generated the i th pixel intensity, y_i , with probability $p(y_i|\sigma_{k_i})$ defined in (2).

Each n th iteration of the EM method is composed of two steps

- *E step*: Where the *expectation* of the new *likelihood* function, $\mathcal{L}(\mathbf{Y}, \mathbf{K}, \Psi)$, is computed with respect to \mathbf{K} ,

$$\mathcal{Q}(\mathbf{Y}, \Psi^n, \Psi) = E_{\mathbf{K}}[\mathcal{L}(\mathbf{Y}, \mathbf{K}(\Psi^n), \Psi)] \quad (6)$$

and

- *M step*: Where a new estimate of Ψ , Ψ^{n+1} , is obtained by maximizing the function \mathcal{Q} ,

$$\Psi^{n+1} = \arg \max_{\Psi} \mathcal{Q}(\mathbf{Y}, \Psi^n, \Psi). \quad (7)$$

These two steps alternate until convergence is achieved, which happens when $|\Psi^{n+1} - \Psi^n| < \xi$, e.g., $\xi = 10^{-3}$.

The *likelihood* function involving all unknowns, visible and hidden, is

$$\begin{aligned} \mathcal{L}(\mathbf{Y}, \mathbf{K}, \Psi) &= \log p(\mathbf{Y}, \mathbf{K}|\Psi) = \sum_{i=1}^N \log p(y_i, k_i|\Psi) \\ &= \sum_{i=1}^N \log p(y_i|\sigma_{k_i}) + \underbrace{\log p(k_i|\sigma_{k_i})}_{\theta_{k_i}}, \end{aligned} \quad (8)$$

where $p(y_i|\sigma_{k_i})|_{k_i=j}$, defined in (2), is the k_i^{th} component of the RMM and θ_{k_i} is the mixture coefficient associated with the k_i^{th} component. The maximization of (8) is impossible because the hidden variables \mathbf{K} are not known. Therefore, the *expectation* with respect to \mathbf{K} is computed as follows,

$$\begin{aligned}\mathcal{Q}(\Psi, \hat{\Psi}) &= E_{\mathbf{K}} [\mathcal{L}(\mathbf{Y}, \mathbf{K}, \Psi) | \mathbf{Y}, \hat{\Psi}] \\ &= \sum_{i=1}^N E_{k_i} [\log p(y_i | \sigma_{k_i}) + \log p(k_i | \sigma_{k_i})] \\ &= \sum_{i=1}^N \sum_{j=1}^L \gamma_{i,j} [\log p(y_i | \sigma_j) + \log \theta_j],\end{aligned}\quad (9)$$

where $\hat{\Psi} = (\hat{\theta}_1, \dots, \hat{\theta}_L, \hat{\sigma}_1, \dots, \hat{\sigma}_L)$ is the previous estimation of the parameters and $\gamma_{i,j}(\hat{\Psi})$ is the distribution of the unobserved variables which is defined as follows,

$$\gamma_{i,j} = p(k_i = j | y_i, \hat{\Psi}) = \frac{p(y_i | \hat{\sigma}_j) p(k_i = j)}{p(y_i | \hat{\Psi})}, \quad (10)$$

where

$$\sum_{j=1}^L \gamma_{i,j} = 1. \quad (11)$$

In (10), $p(y_i | \hat{\sigma}_j)$ is computed as in (2), $p(k_i = j) = \hat{\theta}_j$ and, by definition,

$$p(y_i | \hat{\Psi}) = \sum_{j=1}^L \theta_j p(y_i | \hat{\sigma}_j). \quad (12)$$

The *likelihood* function (9) contains two independent terms, one depending on θ_j and the other on σ_j . Therefore, the function \mathcal{Q} can be minimized independently with respect to each one. The *log-likelihood* function in (9) can be rewritten by separating the terms which depend exclusively on θ_j and σ_j . Taking into account (2) leads to

$$\mathcal{Q}(\Psi, \hat{\Psi}) = \sum_{i=1}^N \sum_{j=1}^L \gamma_{i,j} \log(\theta_j) + \sum_{i=1}^N \sum_{j=1}^L \gamma_{i,j} \left[\log \left(\frac{y_i}{\sigma_j^2} \right) - \frac{y_i^2}{2\sigma_j^2} \right]. \quad (13)$$

Hence, the function \mathcal{Q} can now be minimized independently with respect to θ_j and σ_j .

By using the method *Lagrange multipliers* [29] the term of (13) depending on θ can be maximized under the constraint

$$\sum_{j=1}^L \theta_j = 1. \quad (14)$$

which also provides a necessary condition for optimality in constrained problems [29]. By introducing a new variable (λ) and solving the partial derivative of the term depending on θ , the following expression is obtained,

$$\frac{\partial}{\partial \theta_r} \left[\sum_{i=1}^N \sum_{r=1}^L \gamma_{i,r} \log(\theta_r) + \lambda \left(\sum_r \theta_r - 1 \right) \right] = 0, \quad (15)$$

which leads to

$$\sum_{i=1}^N \gamma_{i,r} = -\lambda \theta_r. \quad (16)$$

By summing both sides of (16) over r ,

$$\underbrace{\sum_{i=1}^N \sum_{r=1}^L \gamma_{i,r}}_{(11)} = -\lambda \underbrace{\sum_{r=1}^L \theta_r}_{(14)}, \quad (17)$$

we get that $N = -\lambda$, which leads to

$$\hat{\theta}_r = \frac{1}{N} \sum_{i=1}^N \gamma_{i,r}. \quad (18)$$

The mixture parameters σ_j are found by differentiating the term in (13), depending exclusively on σ_j , and setting it to zero, as follows,

$$\frac{\partial}{\partial \sigma_r} \left[\sum_{i=1}^N \sum_{r=1}^L \gamma_{i,r} \left(\log \left(\frac{y_i}{\sigma_r^2} \right) - \frac{y_i^2}{2\sigma_r^2} \right) \right] = 0, \quad (19)$$

which is easily solved for σ_r to obtain,

$$\hat{\sigma}_r = \frac{\sum_{i=1}^N \gamma_{i,r} \frac{y_i^2}{2}}{\sum_{i=1}^N \gamma_{i,r}} = \sqrt{\frac{1}{N} \sum_{i=1}^N \gamma_{i,r} \frac{y_i^2}{2}}. \quad (20)$$

The EM algorithm is initialized with L uniformly weighted coefficients $\Theta = \{\theta_j = \frac{1}{L}\}$ while the mixture parameters are assigned with the *Maximum Likelihood* (ML) estimator [30], $\hat{\sigma}_{ML} = \sqrt{\frac{1}{2N} \sum_{i=1}^N y_i^2}$.

The initial choice of components was set arbitrarily to $L = 10$. However, when $|\sigma_m - \sigma_n| < \varepsilon = 1$ (ad hoc setting), meaning that two distributions are closely similar, with $(m \neq n) = \{1, \dots, L\}$, then $\sigma_j = \frac{\sigma_m + \sigma_n}{2}$ and $\theta_j = \theta_m + \theta_n$. This constraint assures stability of the RMM, particularly, for modeling plaque echo-morphology. Preliminary observations allowed to verify that $L = 10$ is an overestimated guess (excessive number of mixture components) which has also implications in the

computational cost of the RMM algorithm. The study of an effective input value for the number of mixture components to be used in the plaque characterization problem is further investigated in Sects. 3.3 and 3.4.

In the next section of experimental results the RMM will be applied in the scope of atherosclerotic plaque characterization and classification for diagnosis purposes.

3 Experimental Results

In this section we first provide a description of the methods used to acquire and process the IVUS data and we briefly introduce the classification framework adopted for tuning the RMM algorithm and performing plaque characterization. Then, two distinct experiments are conducted. The first studies the adequacy of the RMM for describing different tissue types. This experiment is designated as *monolithic description* since the mixture model is estimated by considering all the pixels enclosed in the plaque. The second experiment refers to plaque characterization made pixel-by-pixel (hence, called *plaque local characterization*), where the RMM is applied not to the entire plaque but to each processing block centered at the pixel to be characterized. In order to apply the RMM technique on a classification problem, in local basis, the RMM must be estimated locally and descriptive features must be extracted. Given the envelope image (cf. Sect. 3.1), local RMM features are computed by means of a $K_s \times K_s$ sliding window, moved by a step of $S = \frac{3}{4}K_s$. For each position, a $2L + 1$ -feature array is obtained and presented in the following manner: the first L positions correspond to the Rayleigh parameters sorted in ascending order, followed by the L respective coefficients, arranged accordingly. The last position corresponds to the number of effective mixture components, $\tau = \{1, \dots, L\}$.

The ability of the RMM for local characterization of plaque composition is evaluated when using only the RMM features and when combining them with other texture and spectral features recently proposed in [27].

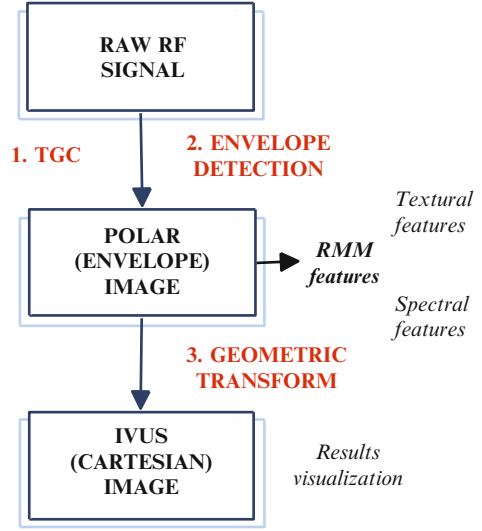
Finally, we present a statistical analysis that supports the relevance of the obtained classification improvement when using the RMM features.

3.1 In-Vitro Data Processing

The adequacy of the proposed RMM to describe real tissue types is evaluated through an in-vitro study of atherosclerotic plaques from an IVUS database. The IVUS data set has been recently presented in [27] and consists of 8 post-mortem arteries, resulting in 45 frames with 24 fibrotic, 12 lipidic and 31 calcified plaques. This data set, composed of 67 plaques, has been validated by histological analysis.

Real-time Radio-Frequency (RF) data acquisition has been performed with the Galaxy II IVUS Imaging System (Boston Scientific) with a catheter Atlantis SR Pro

Fig. 4 IVUS data processing
(see text for details)



40 MHz (Boston Scientific). To collect and store the RF data the imaging system has been connected to a workstation equipped with a 12-bit Acquiris acquisition card with a sampling rate of 200 MHz. The RF data for each frame is arranged in a data matrix of $N \times M$ samples, where $M = 1,024$ is the number of samples per *A-line*, and $N = 256$ is the number of positions assumed by the rotational ultrasound probe.

The information encoded in the visual appearance of tissues naturally represents a relevant feature for their description. However, during acquisition the imaging parameters of the IVUS equipment are typically changed to enhance tissue visualization. Hence, parameters like contrast depth and brightness can change from patient to patient or even from image to image. When the IVUS images are then processed for feature extraction, this fact may generate non-comparable features.

To avoid the aforementioned errors and to produce normalized data, the used data follows a rigorous acquisition protocol where the IVUS images have been directly reconstructed from the raw RF signals rather than using the ones produced by the IVUS equipment. For this purpose, we follow the image reconstruction algorithm [27, 31] outlined in Fig. 4. The reconstruction operations are applied to the RF data, where a preliminary Time Gain Compensation (TGC) function is used,

$$\text{TGC}(r) = 1 - e^{-\beta r}, \quad (21)$$

where $\beta = \ln 10^{\alpha f/20}$, α is the attenuation coefficient for biological soft tissues ($\alpha \approx 0.8 \text{ dB/MHz.cm}$ for $f = 40 \text{ MHz}$ [32]), f is the central frequency of the transducer in MHz and r is the radial distance from the catheter in cm. After signal compensation, using TGC, and envelope detection, using the Hilbert transform, the signal processing procedure described in [27] is applied to get the polar

representation of the IVUS image, or simply the envelope image, resulting in a non-compressed, 256×256 pixels image (cf. Fig. 1b). We recall that the polar image is used to estimate the RMM and to extract the corresponding features. To improve the visualization the polar image is transformed to Cartesian coordinates and its pixels intensities are re-scaled to normalize the observed IVUS image.

This data is exclusively used to represent the image and not for feature extraction.

3.2 Classification Framework

As stated before, the weights and parameters of the mixture, whose estimation was early described, are used as features to describe different types of plaque. In order to evaluate the correct model to be used in a multi-class classification framework that has been successfully used in plaque characterization [27]. The role of the classification scheme is twofold: (1) it allows to evaluate the discriminative power of RMM features and (2) it is used to support a cross-validation process, adopted to tune the L parameter (number of mixture components) in RMM model and the kernel size (image window size where the RMM is estimated).

The classification framework is based on [27] for discriminating among fibrotic, lipidic, and calcified plaques. The multi-class problem is tackled by combining binary classifiers in the *Error-Correcting Output Codes* (ECOC) framework [33]. In fact, ECOC is a technique to decompose a multi-class problem into several binary problems. Each binary problem is here solved by using the *Adaptive Boosting* (AdaBoost) classifier [34] where the weak classifiers are *decision stumps* [35].

The classifier performance is evaluated by means of the *Leave-One-Patient-Out* (LOPO) [31] cross-validation technique, where the training set is built by taking at each validation fold, all patients' data except one, used for testing. Note that each patient data may consist of different number of images (hence, different number of plaques).

Performance results are given in terms of Sensitivity: $S = \frac{TP}{TP+FN}$, Specificity: $K = \frac{TN}{TN+FP}$, Precision: $P = \frac{TP}{TP+FP}$, and global Accuracy: $A = \frac{TP+TN}{TP+TN+FP+FN}$, where TP = True Positive, TN = True Negative, FP = False Positive, and FN = False Negative.

3.3 Plaque Monolithic Description with RMM

The first experiment consists of considering a set of fibrotic, lipidic, and calcified plaques from the entire data set, according to histological analysis. Figure 5a–c shows three examples of IVUS images containing one (or more) distinct tissue types.

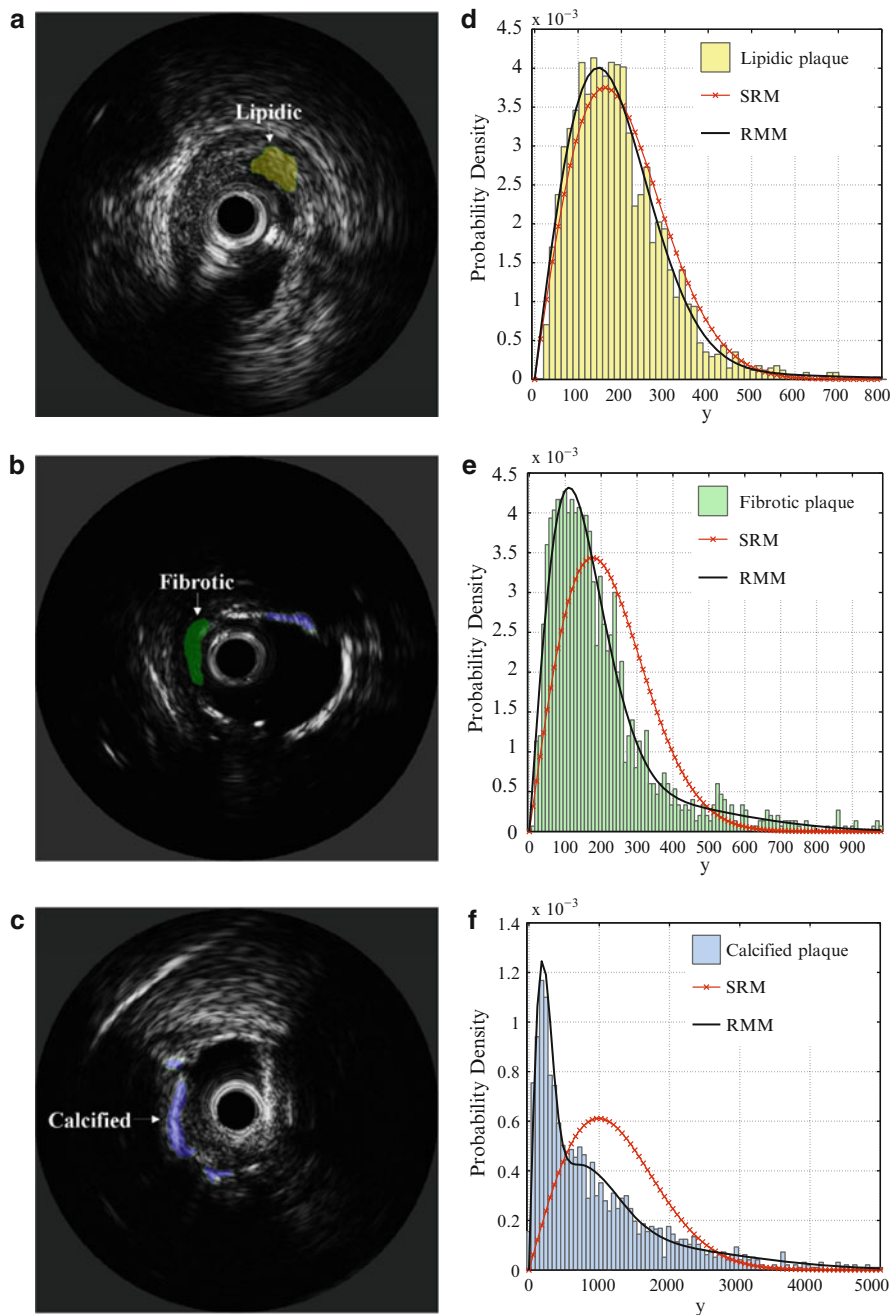


Fig. 5 (a)–(c) RMM modeling of three tissue types. (d)–(f) 3-component mixture PDFs estimated for each tissue type, overlapped with single Rayleigh PDFs

Table 1 Accuracy values for tuning the number of mixture components in RMM (Best performance is indicated in bold)

LOPO	No. mixture components			
(%)	1	2	3	4
A	44.16 (36.28)	68.52 (33.29)	85.56 (18.85)	69.82 (31.00)

Table 2 Performance of RMM, SRM, and median features for monolithic classification (Performance of RMM presented in bold)

LOPO (%)	S_{fib}	S_{cal}	S_{lip}	A
Median	65.00 (39.09)	81.53 (20.34)	44.00 (37.82)	66.30 (15.92)
SRM	41.67 (46.85)	0.00 (0.00)	90.42 (15.84)	44.16 (36.28)
RMM	91.67 (13.94)	93.75 (15.30)	82.00 (24.90)	85.56 (18.85)

The purpose of the current study is to verify the ability of the RMM to describe and distinguish among the three different tissue types. In this particular experiment, the RMM algorithm is applied to the entire set of pixels enclosed in each plaque. Given this, the monolithic plaque area can be characterized by a unique set of RMM features which define a unique plaque type.

Note that this global monolithic approach differs from the other one, described in the next section, where a local analysis make it possible to detect different overlapped types of plaques in the same image. In that approach mixtures are estimated over the pixels of a sliding window the sweeps the whole image.

The classification framework is used to tune the parameters of the RMM method. The most critical parameter to be defined is the number of components to use in the mixture model. In order to determine the optimal L value, we use the LOPO cross-validation method where the classification accuracy is considered as the parameter to maximize.

For each plaque, we apply the RMM algorithm for different number of mixture components from $L = 1$ to $L = 10$. This process results in a set of features having different lengths. For instance, for $L = 3$ we get a 7-length feature vector whereas for $L = 4$ we get a feature vector with 9 elements for each plaque. The training sets composed of RMM features created with $L = (1, \dots, 10)$ are used in the cross-validation process. Results, reported in Table 1, show that the best accuracy is achieved when 3 Rayleigh PDFs (components) are used in the mixture model. Therefore we will use 3 components for this specific plaque classification application. For the sake of simplicity, since classification performance decreases substantially for $L > 4$, we only show the obtained results with L varying from 1 to 4.

In order to demonstrate the effectiveness of RMM when compared to the single distribution, here termed *Single Rayleigh Model* (SRM), or the median gray intensity, we show on Table 2 a comparison of these three types of features for classifying monolithic plaques. The single parameter estimation of the SRM, obtained with the ML criterion [30], is given by $\hat{\sigma}_{ML} = \sqrt{\frac{1}{2N} \sum_{i=1}^N y_i^2}$, where y_i is

Table 3 Kullback–Leibler divergence tests using RMM and SRM: geometric mean computed over 67 plaques

KL	Calcified	Fibrotic	Lipidic
RMM	1.77E-4	7.68E-4	2.20E-3
SRM	1.62E-3	4.93E-3	6.54E-3

Table 4 Mean values of Rayleigh parameters and Mixture coefficients estimated with RMM applied for the data set of 67 plaques

RMM	Components	Lipidic	Fibrotic	Calcified
Rayleigh parameters	1	188	140	318
	2	410	275	1171
	3	–	555	3390
Mixture coefficients	1	0.82	0.51	0.33
	2	0.18	0.39	0.46
	3	–	0.10	0.21

the intensity of the i^{th} pixel within the plaque. It is clear that the application of RMM outperforms the classification results obtained with the other tested features (note that the SRM completely fails in identifying calcified plaques).

Figure 5d–f shows normalized data histograms of lipidic, fibrotic, and calcified tissues, together with the estimated mixture (RMM) and single (SRM) distributions, respectively. Visually, the mixture model composed of three components (early determined to be the best value) describes significantly better the data when compared to the single distribution. Interestingly, as we move from lipidic to fibrotic and calcified tissue, the difference between the mixture distribution and the single distribution increases. At this point, we quantify the adequacy of the mixture model for describing each type of tissue. For this purpose, the mixture and single distributions were estimated for each plaque and the *Kullback–Leibler* (KL) divergence [36] of such distributions with respect to the data was computed. Hence, the smaller the KL divergence is between a given distribution and the data, the more similar they are. We summarize the results by computing the geometric mean of the KL divergence for RMM and ML distributions for each plaque (Table 3).

Observations made in Fig. 5, supported by the results presented in Table 3 reinforce the idea that a single distribution is not sufficient to describe the data, suggesting that different plaque types can be correctly described with different mixture distribution (and thus different RMM parameters). This fact confirms the usefulness of RMM in a tissue modeling problem.

The RMM estimation algorithm is applied to the entire data set, where for each plaque the RMM takes into account all the pixels enclosed in it. The obtained RMM features are presented in Table 4. Particularly, it is observed that lipidic plaques are well described by 2 mixture components, while calcified and fibrotic plaques are modeled by 3 components, where the main difference lies in the range of estimated Rayleigh parameters (Table 4). It is worth noting that in fibrotic tissue estimation the “peakedness” of the single Rayleigh distribution is lower than the observed histogram. There is, indeed, a considerable amount of pixels with high intensity

which means that the maximum likelihood parameter of the Rayleigh distribution (computed as in Sect. 3.3) has a higher value than the expected. As a consequence, the shape of the single Rayleigh distribution will move slightly toward the right direction, as observed in Fig. 5e. This fact enforces the need for a mixture model to correctly model tissues.

The main conclusions that can be obtained from these results are:

1. Lipidic tissues are predominantly modeled by a single Rayleigh distribution. The KL divergence is of the same order for SRM and RMM (see Table 3) and the optimum order of the mixture is one (see Table 4).
2. Fibrotic tissues are approximately described by a mixture of second order.
3. Calcified tissues are better described by three components.
4. There is no significant overlapping between the range of Rayleigh parameters obtained for the lipidic and fibrotic tissues when compared to calcified tissues.

3.4 *Plaque Local Characterization*

We have established the usefulness of using a mixture of distributions to model the plaque content in a monolithic experiment. It is worth to note that, in practice, plaques are not individually segmented, thus the RMM estimation considering all the pixels enclosed in the plaques is not generally a feasible method for plaque characterization. Nevertheless, a region of interest which includes the plaque(s) can be at least pointed out by the physician without compromising the time of a diagnostic exam. Thus, a local-wise characterization, made pixel-by-pixel, becomes a natural and more appropriate strategy. This strategy consists in estimating the RMM over successive processing blocks within the plaque region and assigning the RMM features to each center pixel. Subsequently, each pixel is classified into a specific tissue type (lipidic, fibrotic, or calcified) and then confronted with the ground truth.

As previously mentioned, in order to apply the RMM algorithm to a local analysis, we first need to define the dimension of the kernel to be used. The computational cost associated with the local-wise estimation of RMM features using a processing block (kernel) of size k_s is $\mathcal{O}(2k_s)$. The tuning of this critical parameter is performed again by means of the cross-validation process. For this purpose, the RMM-based features are computed inside a kernel of size $k_s = \{2, 4, 8, 16, 24, 32\}$. Hence, 6 different data sets have been obtained, and for each one of them the cross-validation has been performed, while varying the number of mixture components $L = \{2, 3, 4\}$. Results in terms of global accuracies are depicted in Fig. 6. Given the obtained results, $k_s = 16$ and $L = 3$ are adopted. Hence, the length of the RMM-based feature set extracted from each kernel is $2L + 1 = 7$.

In order to assess the true contribution of the proposed RMM algorithm, the plaque characterization problem is solved under three different conditions, where distinct features were computed from polar RF data (cf. Fig. 4). First, only the RMM

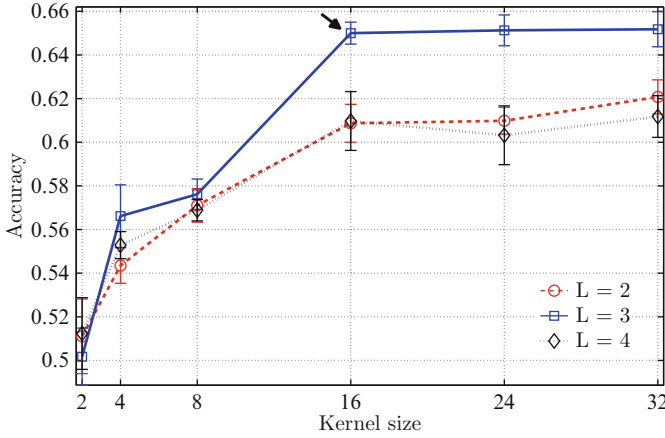


Fig. 6 Classification based on RMM features according to the kernel size and number of mixture components

features are used for tissue discrimination in the classification framework: the obtained classifier is here named *C.1*. Then, a set of 51 textural and spectral features presented in [27] is used to train a second classifier (*C.2*). Finally, RMM features are joined to the textural and spectral features, thus creating a 59-element feature vector, used to train a third classifier (*C.3*).

The three classifiers are used to characterize the plaques of the database according to the LOPO technique. At each fold of both training and validation process, the data set for each kind of plaque has been randomly down-sampled up to the maximum value of the less represented class over all the cases (around 2,000 points per class) in order to obtain a balanced data set among classes.

For each cross-validation fold we compute the aforementioned performance criteria (cf. Sect. 3.2); consequently, for the entire LOPO experiment (eightfolds) we take the average and standard deviation of the results obtained for each fold. Classification results have been obtained by repeating 20 times the cross-validation and finally by averaging the obtained performance parameters.

The comparison of *C.1*, *C.2*, and *C.3* classifiers gives an important evidence of the effectiveness of the RMM features as well as their discriminative power. Classification results achieved with the proposed classifiers are shown in Fig. 7; a more detailed description is given in Table 5.

The use of features estimated with the RMM (*C.1*) provides good results in terms of calcified and fibrotic sensitivity and overall accuracy. A poor performance in terms of correct detection of lipidic tissue is, however, observed. Nevertheless, this is a meaningful achievement in the context of automatic plaque characterization if we consider that the dimension of the feature set is small and exclusively originated from a data source (envelope image, cf. Fig. 4). The combination of the proposed RMM features (*C.1*) with spectral and textural features [27] (*C.2*) is expected

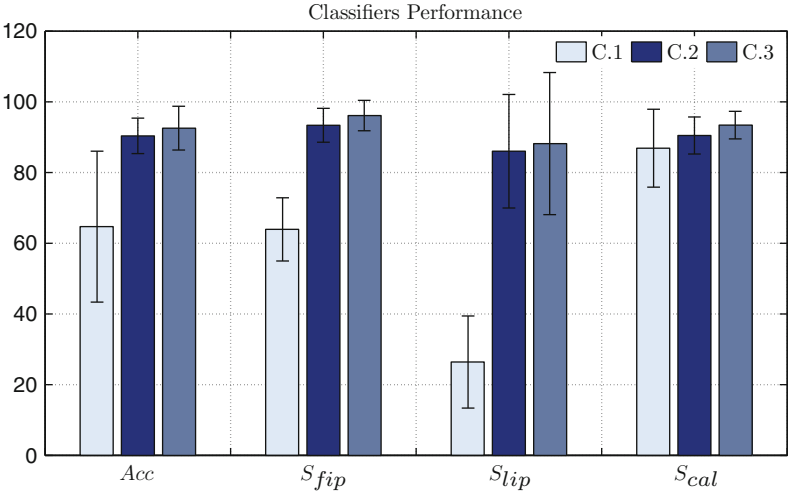


Fig. 7 Bar graph comparing different classifiers (C.1, C.2, C.3) according to performance measures (Acc , S_{lip} , S_{fib} , S_{cal})

Table 5 Performance of plaque characterization: results presented as mean (std)

LOPO (%)	C.1	C.2	C.3
A	64.70 (21.35)	91.37 (5.02)	92.56 (6.18)
S_{fib}	63.93 (8.94)	94.38 (4.79)	96.12 (4.30)
S_{lip}	26.41 (13.03)	87.03 (16.06)	88.19 (20.10)
S_{cal}	86.89 (11.02)	91.48 (5.24)	93.42 (3.90)
K_{fib}	74.68 (25.95)	92.49 (6.22)	94.02 (5.32)
K_{lip}	80.98 (14.59)	97.18 (2.85)	97.69 (3.41)
K_{cal}	94.27 (11.36)	95.22 (5.61)	95.90 (6.85)
P_{fib}	88.55 (11.28)	94.34 (6.74)	95.69 (4.71)
P_{lip}	86.78 (21.06)	69.26 (28.52)	69.71 (29.94)
P_{cal}	94.99 (8.44)	96.89 (3.59)	96.86 (5.18)

to produce improvements on the classification performance. Hence, as shown in Fig. 7 and Table 5, the classifier C.3 yields the best classification accuracy, around 92.6% and brings the class sensitivity up to 96.1%, 88.2%, and 93.4% for fibrotic, lipidic, and calcified plaques, respectively. This represents an improvement of more than 1% in accuracy, about 2% in fibrotic-class, more than 1% in lipidic-class and around 2% in calcified-class sensitivities, when compared to the classifier which only considers textural and spectral features (C.2). These observations support the relevance of the RMM features for plaque characterization.

This result shows that features extracted from RMM are complementary to the rest of the features. Examples of plaque characterization using the C.3 classifier are shown in Fig. 8.

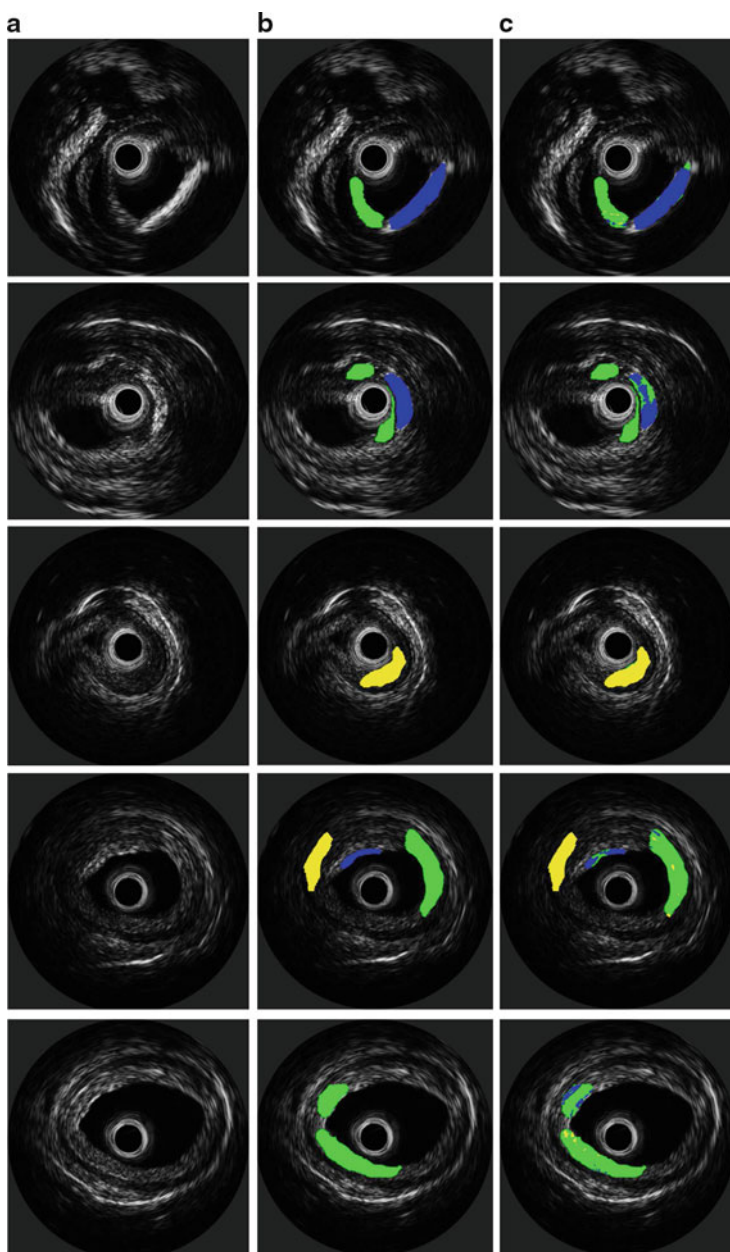


Fig. 8 Examples of plaque classification using the *C.3* classifier. (a) IVUS images, (b) ground truth images, segmented according to the histological analysis, and (c) classification. In *blue* (dark), *green* (mid-gray), and *yellow* (light-gray) are indicated calcified, fibrotic, and lipidic tissues, respectively

Table 6 Mean rank for the accuracy of each classifier

Classifier	C.1	C.2	C.3
Mean rank	2.8438	1.8938	1.2625

3.5 Statistical Analysis

In order to reinforce the usefulness of the RMM approach, we perform a test on the statistical significance of results.

To assess the statistical significance among the classifiers performance, we apply the *Friedman* and *Bonferroni–Dunn* test [37]. First of all, the ranking r_j^i for each separate classification test i and each classifier j is computed. Then, the mean ranking R_j for each one of the j th classifier is computed as $R_j = \frac{1}{\hat{N}} \sum_{i=1}^{\hat{N}} r_j^i$, where $\hat{N} = MN_p$ is the total number of rounds. Obtained results are reported in Table 6. Note that the best rank corresponds to the C.3 classifier, i.e., the classifier trained with the whole feature set.

In addition, in order to reject the *null-hypothesis* that the differences on the measured classification performance are due to randomness, the *Friedman* test is performed. For this purpose, the *Friedman statistic value* is computed,

$$\chi_F^2 = \frac{12\hat{N}}{k(k+1)} \left[\sum_j R_j^2 - \frac{k(k+1)^2}{4} \right], \quad (22)$$

where $k = 3$ is the number of considered classifiers. The obtained value is $\chi_F^2 = 202.74$. As reported in [37], given the conservative property of the Friedman value, the *Iman-Davenport* correction value is preferred,

$$F_F = \frac{(\hat{N} - 1)\chi_F^2}{\hat{N}(k - 1) - \chi_F^2}. \quad (23)$$

The value obtained in this case is $F_F = 274.9$. With three methods and a total of $\hat{N} = 160$ experiments, F_F is distributed according to the F distribution with 2 and 318 degrees of freedom. The critical value of $F(2, \infty)$, for $\alpha = 0.05$ is 2.99. Since the obtained value for F_F is higher than the critical value, the null-hypothesis is rejected, i.e., the differences in the obtained results are not due to randomness.

Once the null-hypothesis has been rejected, we check if the classifier C.3, resulting in the best discriminative power, is significantly better than the other classifiers. For this purpose, the *Bonferroni–Dunn* test [37] is performed. The performance of two classifiers is significantly different if the corresponding average ranks differ by at least the *critical difference*,

$$CD = q_\alpha \sqrt{\frac{k(k+1)}{6\hat{N}}}, \quad (24)$$

where q_α is based on the Studentized range statistic divided by $\sqrt{2}$. Since our goal is the comparison of the *C.3* classifier with respect to the others, the *Bonferroni–Dunn* test is suitable, and a correction factor must be considered in the q_α value (cf. [37] for details). In our case we obtain $CD = 0.2949$ which is smaller than each difference among the mean rank of the classifier *C.3* and the rank of each other classifier. For this reason, we can infer that the classifier is significantly better than the rest with a confidence of 95%.

3.6 Features Weight Analysis

Finally, we want to evaluate the importance of the included features in the quality of the classifier *C.3*. The AdaBoost algorithm [38] assigns a certain weight to each weak classifier selected at each round, during the training process [34]. Since the decision stump weak classifier is only related to a single feature [35], we can use the weight assigned by AdaBoost to evaluate the importance of each feature during the training process. Note that each feature can be selected more than one time: in that case, the sum of each weight for a specific feature is considered.

Let us define N_P the number of in-vitro cases, N_F the number of features, K the number of binary problems, $f = 1, \dots, N_F$ the index of each feature, $k = 1, \dots, K$ the index of each binary problem, N_R the number of rounds by which the computation has been repeated and $\alpha_{k,p,r}^f$ the weight assigned to the f th feature. The normalized weight assigned by AdaBoost to each feature can be computed as $W_f = \max\{w_f^1, \dots, w_f^{N_R}\}$, where

$$w_f^k = \frac{1}{N_P N_R} \sum_{p=1}^{N_P} \sum_{r=1}^{N_R} \frac{\alpha_{k,p,r}^f}{\max\{\alpha_{k,p,r}^1, \dots, \alpha_{k,p,r}^{N_F}\}} \quad (25)$$

In Fig. 9 the normalized weights of each feature are represented together with their detailed description. It is worth to note the importance given by the classifier to the RMM features, particularly to feature #1 (1st Rayleigh parameter), feature #6 (3rd mixture coefficient), and feature #7 (no. effective mixture components). Given the high discriminative power of the *C.3* classifier, the expressive weights assigned to the RMM-based features corroborate the importance of the RMM model, as well as its capability for discriminating different tissues. Hence, this experiment illustrates the relevance of the RMM features for the AdaBoost classifier. Naturally, the information provided about the most discriminant features for classification may be used on a feature selection procedure in future work related to tissue characterization.

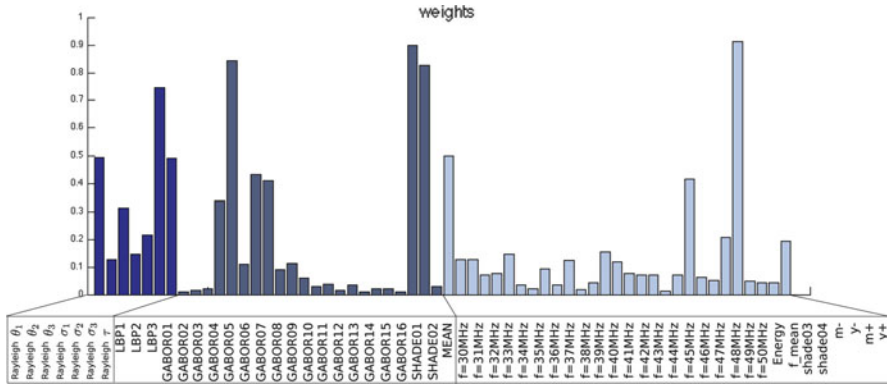


Fig. 9 Analysis of the normalized weight for each feature of the C.3 classifier

4 Conclusions

This chapter proposes a method for plaque characterization in IVUS data based on a mixture of Rayleigh distributions. The coefficients and parameters of the mixture model are used as features for describing fibrotic, lipidic, and calcified plaques.

The RMM algorithm was evaluated and tuned using a classification framework based on a multi-class problem applied to a validated IVUS data set and following a cross-validation strategy. Results suggest that the optimal RMM method for plaque characterization consists of $L = 3$ mixture components and should be computed on a kernel of size $k_s = 16$.

First, the true value of RMM features for tissue characterization was evaluated through a plaque monolithic problem using a cross-validation strategy, providing a global accuracy of 86%. This result highlights the relevance of RMM features for discriminating among the three different types of tissue.

Furthermore, the method was evaluated on a local-wise classification problem when using only the RMM tuned features and when combining them with textural and spectral features used in an authors' previous study. The inclusion of RMM features demonstrates to generally improve the classification performance up to a global accuracy of 92.6%. According to the most significant performance parameters, such as accuracy and class sensitivity, fusing RMM features with textural and spectral features represents a general improvement of more than 1% and in some cases about 2%.

Finally, statistical analysis using the *Friedman and Bonferroni–Dunn* shows that the classifier which includes RMM, textural, and spectral features is significantly better than the other studied ones, thus reinforcing the significance of the obtained improvement when using RMM features.

The analysis of features relevance attributed by AdaBoost demonstrates that the RMM features give an important contribution to the plaque characterization problem.

The method is intended to characterize tissues enclosed in a previously segmented plaque. Moreover, automatic segmentation capabilities can be potentially achieved by classifying the whole image and then by post-processing the labeled regions. Without a deep analysis on features similarities between different vessel areas, the classification result on regions different from plaques cannot be stated. Indeed, it can be guessed that, at least for what concerns the textural features, regions enclosing struts (in presence of stent) can be classified as calcified plaque, and the whole adventitia layer as fibrotic plaque. No guessing can be done for the blood region.

Hence, this chapter has demonstrated that the RMM has a high impact on plaque characterization and could significantly contribute to a more accurate study of plaque composition, and consequently to an objective identification of vulnerable plaques.

References

1. Spagnoli LG (2004) Extracranial thrombotically active carotid plaque as a risk factor for ischemic stroke. *J Am Med Assoc* 292(15):1845–1852
2. Burckhardt C (1978) Speckle in ultrasound B-mode scans. *IEEE Trans Son Ultrason* SU-25(1):1–6
3. Nicolaides AN, Kakkos SK, Griffin M, Sabetai M, Dhanjil S et al (2005) Severity of asymptomatic carotid stenosis and risk of ipsilateral hemispheric ischaemic events: results from the ACSRS study. *Eur J Vasc Endovasc Surg* 30(3):275–284
4. Loizou CP, Pattichis CS (2008) Despeckle filtering algorithms and software for ultrasound imaging. Morgan & Claypool, San Rafael
5. Loizou CP, Pattichis CS, Christodoulou CI, Istepanian RSH, Pantziaris M (2005) Comparative evaluation of despeckle filtering in ultrasound imaging of the carotid artery. *IEEE Trans Ultrason Ferroelectrics Freq Contr* 52(10):1653–1669
6. Sanches JM, Nascimento JC, Marques JS (2008) Medical image noise reduction using the sylvester-lyapunov equation. *IEEE Trans Image Process* 17(9):1522–1539
7. Szabo TL (2004) Diagnostic ultrasound imaging: inside out. Academic, New York
8. Thijssen J (2003) Ultrasonic speckle formation, analysis and processing applied to tissue characterization. *Pattern Recogn Lett* 24(4–5):659–675
9. Diethrich E et al (2007) Virtual histology intravascular ultrasound assessment of carotid artery disease: the carotid artery plaque virtual histology evaluation (CAPITAL) study. *J Endovasc Therap* 14(5):676–686
10. Gussenhoven E, Essed C, Fritman P (1989) Intravascular ultrasonic imaging: histologic and echographic correlation. *Eur J Vasc Surg* 3:571–576
11. Mintz GS, Nissen SE, Anderson WD (2001) American college of cardiology clinical expert consensus document on standards for acquisition, measurement and reporting of intravascular ultrasound studies (ivus). *J Am College Cardiol* 37:1478–1492
12. Zhang X, McKay CR, Sonka M (1998) Tissue characterization in intravascular ultrasound images. *IEEE Trans Med Imag* 17(6):889–899
13. Pujol O, Rosales M, Radeva P, Nofrerias-Fernandez E (2003) Intravascular ultrasound images vessel characterization using adaboost. In: Functional imaging and modelling of the heart: lecture notes in computer science, pp 242–251
14. Granada J et al (2007) In vivo plaque characterization using intravascular ultrasound virtual histology in a porcine model of complex coronary lesions. *Arterioscler Thromb Vasc Biol* 27(2):387–393

15. Nair A, Kuban B, Tuzcu E, Schoenhagen P, Nissen S, Vince D (2002) Coronary plaque classification with intravascular ultrasound radiofrequency data analysis. *Circulation* 106:2200–2206
16. DeMaria A, Narula J, Mahamud E, Tsimikas S (2006) Imaging vulnerable plaque by ultrasound. *J Am College Cardiol* 47(8):32–39
17. Sathyanarayana S, Carlier S, Li W, Thomas L (2009) Characterisation of atherosclerotic plaque by spectral similarity of radiofrequency intravascular ultrasound signals. *EuroIntervention* 5(1):133–139
18. Lopes A, Touzi R, Nezry E (1990) Adaptive speckle filters and scene heterogeneity. *IEEE Trans Geosci Remote Sens* 28(6):992–1000
19. Eltoft T (2006) Modeling the amplitude statistics of ultrasonic images. *IEEE Trans Med Imag* 25(2):229–240; Comparative Study.
20. Prager RW, Gee AH, Treece GM, Berman LH (2003) Decompression and speckle detection for ultrasound images using the homodyned k-distribution. *Pattern Recogn Lett* 24(4–5):705–713
21. Jakeman E (1984) Speckle statistics with a small number of scatterers. *Optic Eng* 23:453–461
22. Dutt V, Greenleaf JF (1994) Ultrasound echo envelope analysis using a homodyned k distribution signal model. *Ultrason Imag* 16(4):265–287
23. Shankar PM (2001) Ultrasonic tissue characterization using a generalized Nakagami model. *IEEE Trans Ultrason Ferroelectrics Freq Contr* 48(6):1716–1720
24. Dempster AP, Laird NM, Rubin DB (1977) Maximum likelihood from incomplete data via the EM algorithm. *J Roy Stat Soc Ser B* 39:1–38
25. Gallaudet T, de Moustier C (2003) High-frequency volume and boundary acoustic backscatter fluctuations in shallowwater. *J Acoust Soc Am* 114(2):707–725
26. Sorensen K, Andersen S (2007) Rayleigh mixture model-based hidden markov modeling and estimation of noise in noisy speech signals. *IEEE Trans Audio Speech Lang Process* 15(3):901–917
27. Ciompi F, Pujol O, Gatta C, Rodriguez O, Mauri F, Radeva P (2009) Fusing in-vitro and in-vivo intravascular ultrasound data for plaque characterization. *Int J Cardiovasc Imag* (formerly cardiac imaging) 26(7):763–779. doi:10.1007/s10554-009-9543-1.
28. Sehgal C (1993) Quantitative relationship between tissue composition and scattering of ultrasound. *Acoust Soc Am J* 94:1944–1952
29. Hadley G (1964) *Nonlinear and dynamic programming*. Addison-Wesley, Reading
30. Harris JW, Stocker H (1998) Maximum likelihood method In: *Handbook of mathematics and computational science*. Springer, New York, p 824
31. Caballero KL, Barajas J, Pujol O, Rodriguez O, Radeva P (2007) Using reconstructed ivus images for coronary plaque classification. In: *Proceedings of IEEE international conference on engineering in medicine and biology, Cit Internationale, Lyon, France*, pp 2167–2170
32. Rosales M, Radeva P (2005) A basic model for IVUS image simulation. In: *Handbook of biomedical image analysis, Topics in biomedical engineering international book series*. Springer, New York, pp 1–55
33. Dietterich TG, Bakiri G (1995) Solving multiclass learning problems via error-correcting output codes. *J Artif Intell Res* 2:263–286
34. Schapire RE (1997) Using output codes to boost multiclass learning problems. In: *Proceedings of 14th international conference on machine learning*. Morgan Kaufmann, CA, pp 313–321
35. Rennie J (2003) Boosting with decision stumps and binary features. Technical report, MIT, MA
36. Cover TM, Thomas JA (1991) *Elements of information theory*. Wiley-Interscience, NY
37. Demšar J (2006) Statistical comparisons of classifiers over multiple data sets. *J Mach Learn Res* 7:1–30
38. Schapire RE (2001) The boosting approach to machine learning: an overview. In: *MSRI workshop on nonlinear estimation and classification*. Berkeley, CA, USA

Ultrasound Imaging

Advances and Applications

Sanches, J.M.; Laine, A.F.; Suri, J.S. (Eds.)

2012, XI, 360 p. 133 illus., 74 illus. in color., Hardcover

ISBN: 978-1-4614-1179-6